ACS APPLIED MATERIALS & INTERFACES

Research Article

www.acsami.org

Multifunctional Metal–Organic Framework Nanoprobe for Cathepsin B-Activated Cancer Cell Imaging and Chemo-Photodynamic Therapy

Jintong Liu, Lei Zhang, Jianping Lei,* Hong Shen, and Huangxian Ju

State Key Laboratory of Analytical Chemistry for Life Science, School of Chemistry and Chemical Engineering, Nanjing University, Nanjing 210023, P. R. China

Supporting Information

ABSTRACT: Integration of a photodynamic therapy platform with a drug-delivery system in a porous structure is an urgent challenge for enhanced anticancer therapy. Here, an amino-functionalized metal–organic framework (MOF), which is useful as efficient delivery vehicle for drugs and provides the $-NH_2$ group for postsynthetic modification, is chosen and well-designed for cell imaging and chemo-photodynamic therapy. The multifunctional MOF nanoprobe was first assembled with camptothecine drug via noncovalent encapsulation and then bound with folic acid as the targeted element and chlorine e6 (Ce6)-labeled CaB substrate peptide as the recognition moiety and signal switch. The designed MOF probe can realize cathepsin B-activated cancer cell imaging and chemo-photodynamic dual-therapy combining Ce6 as the photosensitizer and the camptothecine drug. Compared with the individual treatment, the dual-functional nanoprobe presents an enhanced treatment efficiency in terms of the time of chemotherapy, laser power, and irradiation time of the photodynamic therapy, which has been confirmed in cancer cells and in vivo assays. This work presents a significant example of the MOF nanoprobe as an intracellular switch and shows great potential in cancer cell targeted imaging and multiple therapies.

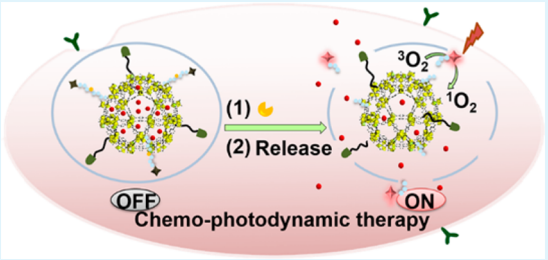

KEYWORDS: *metal–organic frameworks, functionalization, therapy, cell imaging, biosensors*

INTRODUCTION

Metal–organic frameworks (MOFs) are a burgeoning class of crystalline porous compounds constructed of metal ions and organic linkers,[1,2] whose properties can be easily tuned due to the diversity of the constitutional unit.[3−7] In particular, nanoscaled MOFs have been widely utilized in catalysis,[8−10] separation,[11,12] chemical sensors,[13−16] and the loading,[17−19] storage,[20−22] and delivery[23−27] of functional molecules. To efficiently apply the MOFs in biological systems, precise chemical modification is necessary, which provides the possibility to endow MOFs with specific functions and sufficient biocompatibility. To date, different strategies such as dopant modification, postsynthetic methods for subsequent chemical grafting, and entrapping functional molecules in the frameworks have been identified to modify MOFs for signal-transduction and cancer therapy.[28,29] For example, a platinum nanoparticle-encapsulated MOFs is developed as a smart tracer for the electrochemical detection of telomerase activity.[30] The iron–carboxylate MOFs functionalized by postsynthetic modifications have been designed for anticancer through delivering an imaging agent and drugs via the decomposition of the particles.[31] Different from other nanomaterials such as polymer micelles, nanoparticles, and graphene oxide,[32−34] the MOFs provide the abundant modification sites for simultaneous assembling with the signal recognition element and the drug moiety. Therefore, it is desirable for the assembly of MOF structures with multitudinous biomolecules to realize their multifunctions in clinical applications, especially in cell imaging and therapy.

Considering the varieties of cancers, four therapeutic techniques, such as surgical resection, chemotherapy, photodynamic therapy (PDT), and photothermal therapy, are involved in the treatment of cancers. However, on the one hand, the resistance and side effects of multidrugs may restrict the potential of chemotherapy.[35] On the other hand, PDT has predominant advantages over other traditional therapies due to its noninvasive nature and fast cure process.[36−40] Interestingly, Lin's group developed brilliant advances about porphyrin- and chlorin-based MOFs as photosensitizers for tumor therapy.[41,42] Nevertheless, the hypoxia in solid tumors reduces the generation efficiency of reactive oxygen species.[43,44] What's worse, PDT-mediated decrease of O_2 aggravates tumor hypoxia, leading to lower therapy efficiency.[45,46] To overcome the limitations,[47] developing the dual therapeutic modalities integrating chemotherapy and PDT has been illustrated to not only retard drug resistance but also reduce the O_2 dependence for high therapy effectiveness.[48−51] For example, a coordination polymer core–shell nanoparticle was developed for carrying cisplatin and the photosensitizer to synergistically induce cancer cell apoptosis.[52] The processes of the above therapies were controlled by folic acid receptor (FR)-based

Received: November 11, 2016
Accepted: December 29, 2016
Published: December 29, 2016

DOI: 10.1021/acsami.6b14446
ACS Appl. Mater. Interfaces 2017, 9, 2150−2158

recognition and triggered by pH response, which has the inherent limitations of single-mode recognition with a background.[32,53,54] Therefore, it is imperative urgently to develop the imaging assessment of the tumor malignancy grade during the process of chemotherapy and PDT. The multifunctional therapy platform integrating the selective target-imaging of cancer cells, feedback, and stepwise therapy provides the possibility for precise therapy.

For this purpose, we focus on the cathepsin B as an intracellular target for a switch of diagnostic imaging to choose different therapies. CaB is a kind of lysosomal cysteine endopeptidase and shows increased expression in many types of cancer, providing a significant principle to trigger cancer theranostics.[55−59] In this work, a functionalized MOF nanoprobe as the drug carrier, postsynthetic modification site, and quenching reagent was designed for in situ CaB-activatable cancer cell imaging and synergistic chemo-photodynamic therapy (Scheme 1). The multifunctional MOF nanoprobe

Scheme 1. Schematic Illustration of (A) Preparation of Multifunctionalized CPC@MOF Nanoprobe and (B) Cathepsin B-Activated Cancer Cell Imaging and Chemo-Photodynamic Therapy

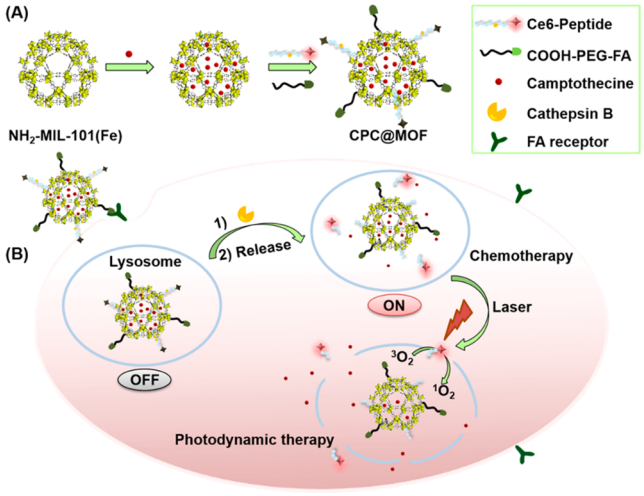

(CPC@MOF) was first encapsulated with camptothecine (Cam) in the nontoxic iron(iii) carboxylate MOFs (NH_2-MIL-101(Fe), MIL = Materials of Institut Lavoisier)) via noncovalent interaction, and then it assembled with folic acid (FA) as the targeted element and chlorine e6 (Ce6)-labeled CaB substrate peptide (Ce6-peptide) as the signal and recognition moiety and photosensitizer. Upon FR-mediated endocytosis, the drug (Cam) loaded in the MOF could introduce the chemotherapy. Meanwhile, the Ce6 fluorescence was recovered due to its detachment from the MOF surface after the specific cleavage reaction of intracellular CaB to Ce6-peptide, resulting in a sensitive way for specific imaging of intracellular CaB. Once the imaging of cancer indicates the highly severe grade tumor, the 660 nm laser irradiation could be further used for irradiating the released Ce6 to generate $^1O_2$ for the PDT. Therefore, a highly effective synergistic chemo-photodynamic therapy and target-activated cancer cell imaging can be achieved by the designed CPC@MOF. Moreover, the dual-therapy platform could be delivered to different sites in cancer cells with stepwise therapeutic modalities. This multifunctional MOF probe realizes cancer-cell target delivery, CaB-activited imaging, and integrative treatment of chemo-photodynamic therapy, providing a promising approach for assessment and choice of therapy modalities in clinical diagnosis.

EXPERIMENTAL SECTION

Synthesis of MOF-NH_2 and Cam@MOF. The NH_2-MIL-101(Fe) (MOF-NH_2) was synthesized according to the previous study with some modifications.[26] Briefly, a mixture of 18 mg of aminoterephthalic acid (NH_2−BDC) and 27 mg of $FeCl_3{\cdot}6H_2O$ in 5 mL of water was placed into microwave under 400 W at 60 °C for 5 min. The mixture was cooled and precipitated by centrifugation at 10 500 rpm for 10 min. The resulting solid was washed and dried in a vacuum to obtain MOF-NH_2.

Subsequently, Cam was encapsulated into MOF-NH_2 to obtain Cam@MOF conjugate by postsynthetic method. That is, 10 mg of MOF-NH_2 was added into the 1 mL Cam solution (1 mg mL^{-1}). The mixture was stirred at room temperature for 36 h. Nine milliliters of solution containing HOOC-poly(ethylene glycol) (PEG)-FA (0.5 mg), 1-ethyl-3-(3-(dimethylamino)propyl)carbodiimide hydrochloride (EDC) (10 mg), and N-hydroxysuccinimide (NHS) (20 mg) was gently shaken at room temperature for 40 min, added into the resulting MOF solution, and then incubated at room temperature for 3 h. The amount of Cam in the MOF-NH_2 was calculated according to a calibration curve of Cam (Figure S2).

Synthesis of Ce6@MOF and CPC@MOF. EDC (10 mg) and NHS (20 mg) were added to 9 mL of 40 μM Ce6-peptide solution containing 0.5 mg of HOOC-PEG-FA. After the mixture was gently shaken at room temperature for 40 min, MOF-NH_2 solution (1 mL; 10 mg mL^{-1}) was injected into this mixture and incubated at room temperature for 3 h. This solution was concentrated by centrifugation and washed with water twice. Thus, the functionalization of MOF-NH_2 with HOOC-PEG-FA and Ce6-peptide (Ce6@MOF) was obtained and then resuspended in pH 7.4 phosphate-buffered saline (PBS) for further experiments. According to the method described above, the CPC@MOF was similarly synthesized using the Cam@MOF instead of MOF-NH_2.

Confocal Fluorescence Imaging and Flow Cytometric Assay. HeLa or HaCaT cells were incubated with Ce6@MOF (1.6 μM Ce6 equiv) at 37 °C for 7.5 h and rinsed three times with PBS. Prior to confocal fluorescence imaging, the cells were irradiated with a 660 nm laser for 5 min. The fluorescence of cells was collected from 645 to 700 nm on the microscope with the excitation wavelength of 633 nm. Flow cytometry was used to evaluate the specificity of the probe to cancer cells. After treatment with the probe as described above, cells were trypsinized, harvested, rinsed with PBS, and resuspended, and flow cytometric assay was conducted over FL4 channel.

Therapeutic Monitoring. HeLa cells were seeded into confocal dishes and incubated for 24 h at 37 °C. When the confluency of the cells was ∼70%, the medium was then replaced with culture medium containing MOF-NH_2, Ce6@MOF, Cam@MOF, or CPC@MOF, individually, and incubated at 37 °C for 7.5 h. After the irradiation with or without a 660 nm laser at a power of 200 mW cm^{-2} for 5 min, the morphology and fluorescence of cells was collected on a confocal laser scanning microscope.

For flow apoptosis cytometric evaluation, HeLa cells were seeded in a six-well plate for 12 h containing 2 mL of fresh Dulbecco's modified Eagle's medium in each well. These cells were then incubated with different probes as described above for 7.5 h and then treated with or without laser irradiation for 5 min. The resulting cells were collected, stained with the mixture of 5.0 μL of Annexin V-FITC and 5.0 μL of propidium iodide (PI) for 15 min, and analyzed with flow cytometry over FL1 (Annexin V-FITC) and FL3 (PI) channels.

Animal Experiments. The animal operations were performed with the requirements of institutional animal use and care approved by the Model Animal Research Center of Nanjing University. Specific pathogen-free HeLa-tumor mice were bred for this experiment and injected with CPC@MOF (1.6 μM Ce6 equiv). In the time-dependent assays, a tumor-bearing mouse was injected with CPC@MOF (1.6 μM Ce6 equiv) via tail vein, and measurement was conducted on a

DOI: 10.1021/acsami.6b14446
ACS Appl. Mater. Interfaces 2017, 9, 2150−2158

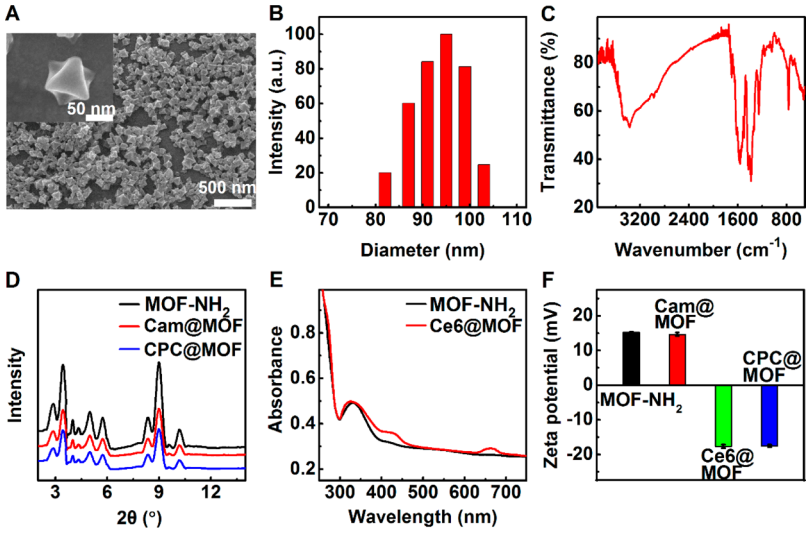

Figure 1. (A) SEM image of MOF-NH_2. (inset) Amplified image. (B) DLS assay and (C) IR spectrum of MOF-NH_2. (D) PXRD patterns of MOF-NH_2, Cam@MOF, and CPC@MOF. (E) UV−vis absorption spectra of MOF-NH_2 and Ce6@MOF. (F) Zeta potential of MOF-NH_2, Cam@MOF, Ce6@MOF, and CPC@MOF.

Maestro Imaging System. As comparison, PBS, Cam, Ce6-peptide, Cam + Ce6-peptide, Ce6@MOF, and Cam@MOF with laser irradiation were used in the process for evaluating the therapeutic efficiency. The tumor volume was measured by a vernier to measure the tumor volume after treatment. Finally, the excised organs and tumor tissue were obtained after the mice were euthanized for ex vivo imaging.

RESULTS AND DISCUSSION

Structure Characterization and Functionalization. To synthesize CPC@MOF probe, MOF-NH_2 was used as the initial matrix, showing an octahedron morphology in scanning electron microscopy (SEM) images (Figure 1A), and the structure had a hierarchy of mesoporous sizes at ∼2.8 nm (Figure S1). Meanwhile, the dynamic light scattering gave the mean hydrodynamic diameter of 95 nm (Figure 1B), suggesting the potential of application in the intracellular assays. The incorporated ligand of 2-aminoterephthalic acid in the framework was proved by Fourier transform infrared (FT-IR) spectrum, which showed the characteristic bands such as C−O (1576 and 1432 cm^{-1}), amine moieties (3441 and 3379 cm^{-1}), N−H (1623 cm^{-1}), and C−H (1339 cm^{-1}) (Figure 1C).[60] The prepared MOF-NH_2 displayed a typical powder X-ray diffraction (PXRD) pattern (black line, Figure 1D) that closely matched the reported work,[31] implying the successful synthesis of MIL-101-type MOF.

After Cam was loaded into the framework of MOF-NH_2, the resulting Cam@MOF showed the similar XRD curve with the MOF-NH_2 (red line, Figure 1D), manifesting the maintenance of its crystalline structure after drug encapsulation. The payloads of Cam in MOF was estimated to be 3.9 wt % by the fluorescence measurement of Cam (Figure S2). To improve the biocompatibility of the probe, HOOC-PEG-FA was used to protect MOF from aggregation and achieve FR-mediated endocytosis, which was characterized by UV−vis spectrum. After the functionalization of MOF-NH_2 with HOOC-PEG-FA and Ce6-peptide, the absorption spectrum of Ce6@MOF showed the characteristic absorptions at 425 and 660 nm for Ce6-peptide and at 280 and 320 nm for FA (Figure 1E).[61,62] Furthermore, the zeta potential of MOF-NH_2 and Cam@MOF changed from the positive state into negative state (−17.7 mV), after assembling with negatively charged peptides (Figure 1F). The loaded amount of Ce6-peptide on the MOF surface was determined to be 32.3 mg g^{-1} by the measurement of Ce6 fluorescence (Figure S3).

Specific Response to CaB. To verify the Ce6@MOF for intracellular CaB-activable imaging, enzymatic assays in vitro were performed on the fluorescence spectro-photometer. When Ce6-peptide was modified on the MOF surface, the fluorescence intensity of Ce6-peptide was quenched because of the electron transfer from the excited Ce6 to MOF-NH_2 (Figure S4).[63] Upon the incubation with CaB, the fluorescence was recovered, which was attributed to the cleavage of the substrate peptide by CaB to release Ce6 from MOF surface. At the optimized incubation time of 60 min (Figure S5A), the fluorescence intensity increased with the enhanced concentration of CaB (Figure 2A,B). The cleavage reaction showed the optimal dependence in the pH range of 4.5−6.0 (Figure S5B). Thus, pH 5.0 was used for the subsequent experiments in solution considering the lysosome microenvironment. In addition, the cleavage reaction had obvious response and high selectivity for CaB. The addition of the CaB inhibitor could inhibit the fluorescence recovery of Ce6@MOF, indicating the specific activation of Ce6@MOF by CaB. However, the Ce6@MOF showed little change in the presence of cathepsin D (CaD) or cathepsin L (CaL) (Figure 2C).

$^1O_2$ Generation Assays. The $^1O_2$ controlled release should be a significant challenge during the PDT. The $^1O_2$ generation of Ce6@MOF at the absence and presence of CaB with irradiation was monitored with an $^1O_2$ indicator, namely, singlet oxygen sensor green (SOSG; (Figure 2D), which could emit a strong fluorescence at 525 nm after reacting with $^1O_2$.[64] Compared with the Ce6@MOF or Ce6−peptide without irradiation (curves a and b), the mixture of Ce6@MOF and indicator emitted a weak increase of SOSG fluorescence under irradiation (curve c). After CaB was added into the Ce6@MOF solution, the fluorescence intensity was significantly enhanced (curve e), which was caused by the block of electron transfer from Ce6 to the MOF via the cleavage reaction. The similar enhanced fluorescence could be observed in the Ce6−peptide solution after irradiation (curve f). In the presence of CaB

DOI: 10.1021/acsami.6b14446
ACS Appl. Mater. Interfaces 2017, 9, 2150−2158

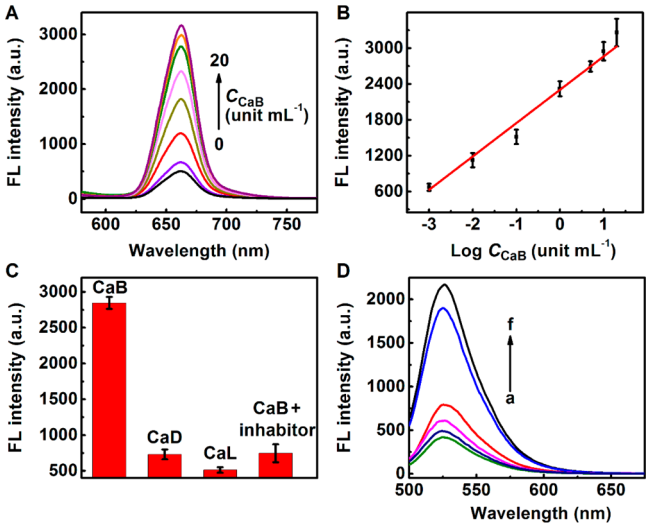

Figure 2. (A) Fluorescence spectra of Ce6@MOF (1.6 μM Ce6 equiv) after incubation with 0, 0.001, 0.01, 0.1, 1.0, 5.0, 10, and 20 unit mL^{-1} CaB in PBS for 60 min. (B) Plot of fluorescence intensity vs the logarithm of CaB concentration. (C) Fluorescence intensity of Ce6@MOF at 660 nm after treated with CaB, CaD, CaL, and the mixture of CaB and inhibitor for 1 h. (D) fluorescence intensity of SOSG at 525 nm treated with Ce6@MOF + CaB (a) and Ce6-peptide (b) without laser irradiation, and Ce6@MOF (c), Ce6@MOF + CaB + inhibitor (d), Ce6@MOF + CaB (e) and Ce6-peptide (f) under laser irradiation. The irradiation was performed by a 660 nm laser with a power of 200 mW cm^{-2}.

inhibitor, the SOSG fluorescence intensity was evidently reduced (curve d). These results manifested the strong $^1O_2$ inhibition ability of MOF and specific response by CaB to induce the $^1O_2$ generation.

Cell Imaging and Colocalization Assays of Ce6@MOF. For in situ imaging, HeLa cells were incubated with Ce6@MOF for conducting confocal fluorescence imaging. After 2.5 h of incubation, the cells showed some detectable fluorescent spots (Figure 3A), demonstrating the quick internalization and

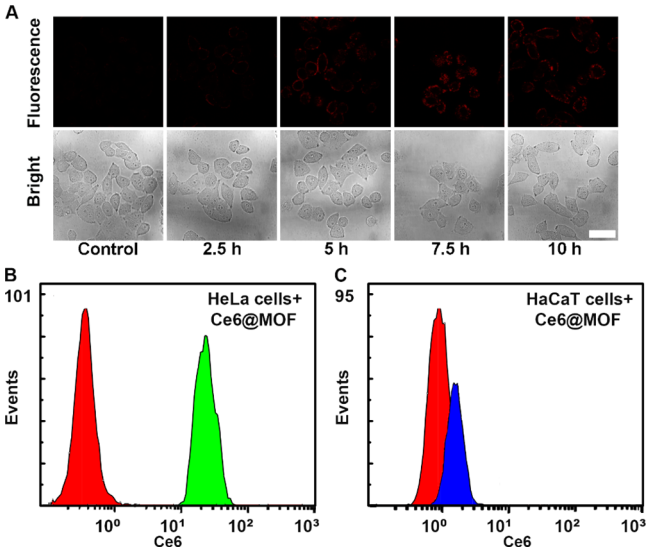

Figure 3. (A) Time course of confocal fluorescence images and bright-field images of HeLa cells. Flow cytometric assay of (B) HeLa cells and (C) HaCaT cells incubated with Ce6@MOF for 7.5 h at 37 °C. Scale bar, 50 μm.

subsequent activation of Ce6@MOF by CaB. The fluorescence enhanced gradually and reached the maximum at 7.5 h. To validate the targeted delivery of Ce6@MOF into cancer cells, FR-positive HeLa cells and FR-negative HaCaT cells were used for this assay. The cells were incubated with the Ce6@MOF for 7.5 h and evaluated via flow cytometric analysis by using the fluorescence of Ce6. Unlike HeLa cells, no obvious fluorescence change was observed from the Ce6@MOF-treated HaCaT cells due to the low expression of FA receptor (Figure 3B,C). Confocal fluorescence imaging assays were performed for further confirming the specificity of Ce6@MOF to cancer cells by the recognition of FA receptor. The probe-incubated MCF-7 and HeLa cells showed detectable Ce6 fluorescence due to the high expression of FA receptor, while no fluorescence was observed in the A549 cells with negative FA receptor (Figure S6). In the colocalization experiments (Figure S7), the red fluorescence of Ce6@MOF overlapped with the lysosomal tracker (LysoTracker Green), manifesting that Ce6@MOF could be delivered into lysosome after internalization and that the fluorescence was recovered by the CaB in the lysosome.

Light and Dark Cytotoxicity. Before investigating the PDT therapeutic agents, the dark and light cytotoxicity of the MOF-NH$_2$, Ce6@MOF, and CPC@MOF to cancer cells was investigated by a standard 3-(4,5-dimethylthiazol-2-yl)-2,5-diphenyltetrazolium bromide (MTT) system (Figures 4 and

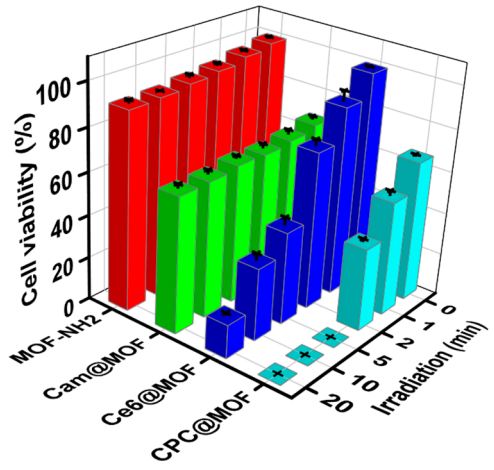

Figure 4. MTT assays of HeLa cells incubated with MOF-NH$_2$, Cam@MOF, Ce6@MOF, CPC@MOF after laser irradiation with a power of 200 mW cm^{-2} at different time.

S8). More than 90% viability of MOF-NH$_2$-incubated HeLa cells treated with/without 660 nm laser irradiation indicated the low cytotoxicity for both MOF skeleton and laser irradiation. After HeLa cells were treated with Ce6@MOF for 7.5 h, the cells could maintain a high viability of 91.1%, suggesting the tolerance of its low dark cytotoxicity. However, the enhanced apoptosis percentage of Cam@MOF or CPC@MOF-treated HeLa cells with the increasing amount of Cam encapsuled in the MOF demonstrated the pharmacological effect of Cam due to the efficient loading/release of Cam (Figure S8). Meanwhile, the viability of the cells treated with Ce6@MOF or CPC@MOF greatly decreased with increasing laser irradiation time due to the recovered photosensitivity of Ce6 cleaved by intracellular CaB (Figure 4). These results demonstrated the low dark cytotoxicity, high light cytotoxicity, and enhanced therapy efficiency of CPC@MOF.

DOI: 10.1021/acsami.6b14446
ACS Appl. Mater. Interfaces 2017, 9, 2150−2158

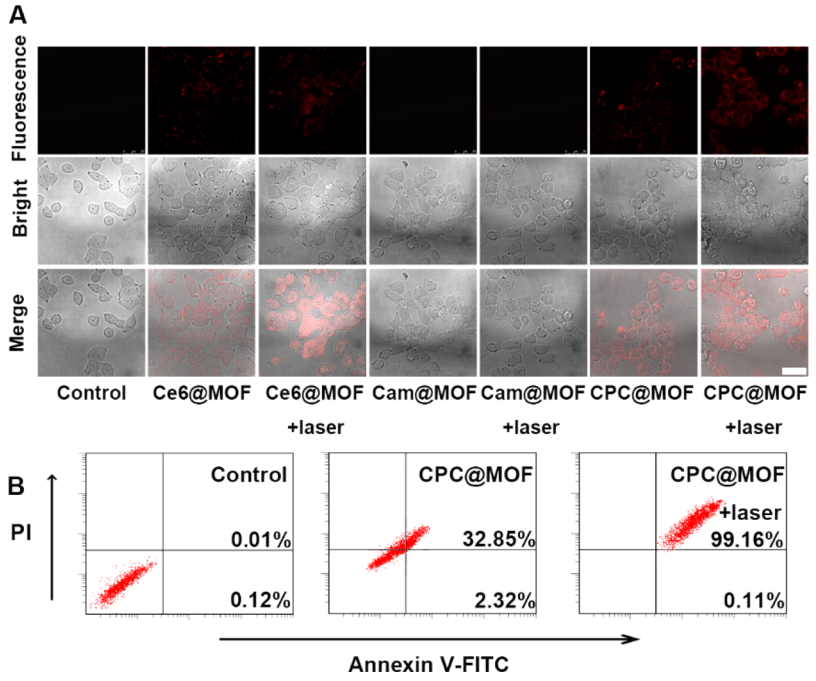

Figure 5. (A) Confocal fluorescence imagings of HeLa cells treated with Ce6@MOF (1.6 μM Ce6 equiv), Cam@MOF, and CPC@MOF for 7.5 h and then irradiated with or without 660 nm laser for 5 min. Scale bar, 50 μm. (B) Flow cytometric analysis of HeLa cells treated with CPC@MOF for 7.5 h before and after laser irradiation using apoptosis kit with the dual fluorescence of Annexin V-FITC/PI.

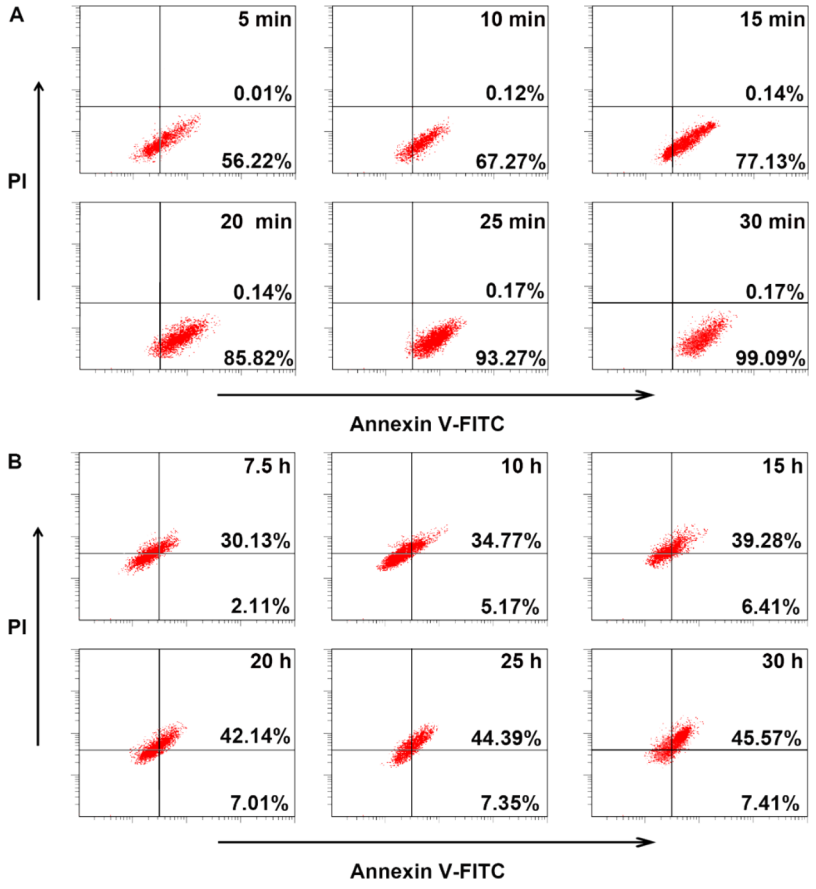

Figure 6. Flow cytometric analysis of HeLa cells by using apoptosis kit with the dual fluorescence of Annexin V-FITC/PI after incubated with (A) Ce6@MOF (1.6 μM Ce6 equiv) for 7.5 h and then irradiated with 200 mW cm^{-2} of laser and (B) Cam@MOF for different time.

Fluorescence Imaging and Chemo-Photodynamic Therapy of CPC@MOF. The confocal imaging of HeLa cells was performed to evaluate the therapeutic effectiveness of Ce6@MOF and CPC@MOF (Figure 5). After a 5 min laser

DOI: 10.1021/acsami.6b14446
ACS Appl. Mater. Interfaces 2017, 9, 2150−2158

post-irradiation of Ce6@MOF-incubated cells for 7.5 h, a few bubbles appeared on the surface of HeLa cells, and the fluorescence spot of Ce6 gradually diffused from lysosomes to cytoplasm resulting from the destruction of lysosome. Meanwhile, the apoptotic apperance of HeLa cells was observed after incubation with Cam@MOF for 7.5 h, at which time Cam showed a considerable release efficiency from the MOF skeleton as a result of the diffusion from the pores and/or drug-matrix interaction (Figure S9). However, no obvious morphological change of Cam@MOF-treated cells occurred under laser irradiation after 7.5 h of incubation, which was caused by the absence of CaB-activated Ce6. To access the collaborative treatment of chemotherapy and PDT, the HeLa cells were incubated with CPC@MOF for 7.5 h and then treated with the laser irradiation for 5 min. On the one hand, lots of bubbles appeared on the cell surface, and the cells exhibited significant morphological change. On the other hand, flow cytometry analysis, which was conducted by Annexin V-FITC together with PI apoptotic kit, was used as dual-fluorescence probe to distinguish viable cells from dead cells after treatment with CPC@MOF (Figure 5B). Combining both chemotherapy and PDT effect of CPC@MOF, a total of 99.27% HeLa cells showed apoptosis under laser irradiation with the power of 200 mW cm^{-2} for 5 min. However, only 35.17% apoptotic percentage of CPC@MOF-treated HeLa cells without laser irradiation could be achieved by the effect of Cam in MOF. These results indicated that chemo-photodynamic therapy of CPC@MOF could achieve a desirable therapeutic efficacy.

Next, a series of flow cytometric apoptosis assay was performed to test the synergistic therapy efficiency of the CPC@MOF (Figure 6). The laser dose including irradiation time and laser power used in the PDT process should be taken into consideration.[37] As shown in Figure 6A, the total apoptosis ratio of the Ce6@MOF-treated Hela cells increased with the exposure time and reached nearly 99.26% until 30 min, which was much longer than the time for CPC@MOF-treated cells (5 min). The assay of the HeLa cells treated with Ce6@MOF displayed growing apoptosis degree under increasing laser power (Figure S10) and gained the satisfactory apoptosis degree at 500 mW cm^{-2}, which was comparable to the effect of CPC@MOF with the power of 200 mW cm^{-2}, demonstrating the good therapy performance of multifunctional CPC@MOF probe. Besides, the treatment time was also an important factor in the therapy process. As shown in Figure 6B for Cam@MOF, 53% apotosis ratio of pure drug-treated HeLa cells needed the long treatment time of 30 h. In comparison, above 99% apotosis ratio of CPC@MOF-treated cells was achieved after 7.5 h of incubation and 5 min of laser irradiation at 200 mW cm^{-2}. These results manifested that a better therapy efficiency could be achieved by the synergistic antitumor effect both the chemotherapy and CaB-depended PDT of CPC@MOF.

In addition, the specificity of the CPC@MOF to cancer cells was investigated in normal HaCaT cells (Figure S11). No obvious cytotoxicity of the cells after treated with CPC@MOF for 7.5 h and then laser exposure for 5 min was observed from normal HaCaT cells, which was attributed to the low expression of FR on HaCat cells surface. Thus, the CPC@MOF probe could be considered as a potential paradigm for targeted therapy against cancer.

In Vivo Therapy on Subcutaneous HeLa Tumor-Bearing Mice. The dual therapy of chemotherapy and PDT by using the CPC@MOF in vivo was assessed by monitoring the tumor volume in living mouse. The HeLa tumor-bearing mice were injected with CPC@MOF for in vivo imaging. The probe accumulated in the tumor gradually and reached to maximum at 24 h postinjection (Figure 7A). In the evaluation

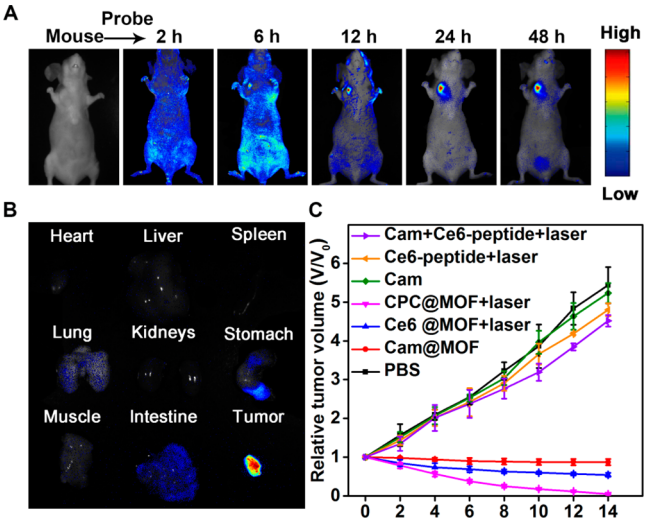

Figure 7. (A) Time-dependent in vivo fluorescence images of subcutaneous HeLa tumor-bearing mouse after injected with CPC@MOF. (B) Ex vivo fluorescence image of organs and cancer tissue from HeLa tumor-bearing mouse treated with 24 h postinjection of CPC@MOF. (C) Change of relative tumor volume after treatment with 24 h postinjection of PBS, Cam, Ce6-peptide, Cam + Ce6-peptide, Cam@MOF, Ce6@MOF, and CPC@MOF.

of excised tissues, the strong fluorescence occurred in the cancer tissue compared with the other organs including spleen and kidneys (Figure 7B), which further demonstrated the CPC@MOF was accumulated in the tumor particularly and the fluorescence was recovered by CaB specific activation. Then 660 nm laser was performed to the mice and irradiated for the PDT. For the comparison purpose, the other tumor-bearing mice were intravenously injected with PBS, Ce6-peptide, Cam, Ce6-peptide + Cam, Ce6@MOF, and Cam@MOF. To estimate the efficacy of CPC@MOF-mediated dual therapy, the tumor volume measurement was conducted for 14 d after treatment (Figure 7C). The PBS group had rapidly promoted volume from the mouse with 24 h postinjection, and the similar results were observed for the Cam, Ce6-peptide, and Ce6-peptide + Cam group due to the lack of targeted delivery. The tumor of Cam@MOF group was slightly inhibited due to the chemotherapeutics. In addition, both the laser irradiation-treated and Ce6@MOF-treated or CPC@MOF-treated mice showed reduced tumor volume, while the ones injected with CPC@MOF appeared much more competent than those with Ce6@MOF. Overall, the designed CPC@MOF had the potential clinical application in CaB-triggered dual therapy of PDT and chemotherapy to overcome the individual drawback in a single therapy against cancers.

CONCLUSION

In summary, a novel MOF-based multifunctional nanoprobe has successfully been constructed by integrating postsynthetic method with entrapping functional molecules in the frameworks for CaB-activatable fluorescence imaging and dual therapeutics of target-controlled PDT and chemotherapy. The multifunctional MOF probe possesses synthetic convenience,

DOI: 10.1021/acsami.6b14446
ACS Appl. Mater. Interfaces 2017, 9, 2150−2158

good biocompatibility, and superior loading effectiveness of the Ce6−peptide and drug molecule. It can be conveniently used for selective cathepsin B responsive imaging and the synergistic chemo-photodynamic therapy against tumor issues with excellent specificity and sufficient efficiency, providing a method for assessment and choice of therapy approach. Moreover, the integration treatment platform reduces side effects, retards multidrug resistance of the chemotherapeutics, and overcomes the low efficiency of the PDT in the hypoxia cells, resulting in significant enhancement in the therapeutic efficacy. The unique inner porosity and postsynthetic easiness endows the MOF nanoprobe with target-cell-specific delivery, in situ imaging, and synergistic therapy for promising application in precise medicine.

■ ASSOCIATED CONTENT

Supporting Information

The Supporting Information is available free of charge on the ACS Publications website at DOI: 10.1021/acsami.6b14446.

Detailed experiments, characterization of MOF-NH_2, calibration curve of Cam and Ce6-peptide, fluorescence response of Ce6@MOF to CaB, optimization of conditions, Ce6@MOF probe-treated different cell lines, colocalization assay, MTT assays, release rate of Cam, effect of laser power, and responses of different MOF probes to HaCaT cells (PDF)

■ AUTHOR INFORMATION

Corresponding Author

*Phone/Fax: +86-25-89681922. E-mail: jpl@nju.edu.cn.

ORCID

Jianping Lei: 0000-0002-3594-180X

Author Contributions

All authors have given approval to the final version of the manuscript.

Notes

The authors declare no competing financial interest.

■ ACKNOWLEDGMENTS

We gratefully acknowledge the National Natural Science Foundation of China (21375060, 21135002, 21675084) and priority development areas of the National Research Foundation for the Doctoral Program of Higher Education of China (20130091130005).

■ REFERENCES

(1) Yaghi, O. M.; Eddaoudi, M.; O'Keeffe, M.; Li, H. L. Design and Synthesis of an Exceptionally Stable and Highly Porous Metal-Organic Framework. *Nature* **1999**, *402*, 276−279.

(2) Furukawa, H.; Cordova, K. E.; O'Keeffe, M.; Yaghi, O. M. The Chemistry and Applications of Metal-Organic Frameworks. *Science* **2013**, *341*, 1230444.

(3) Lee, J. Y.; Farha, O. K.; Roberts, J.; Scheidt, K. A.; Nguyen, S. T.; Hupp, J. T. Metal-Organic Framework Materials as Catalysts. *Chem. Soc. Rev.* **2009**, *38*, 1450−1459.

(4) Wang, Z. Q.; Cohen, S. M. Postsynthetic Modification of Metal-Organic Frameworks. *Chem. Soc. Rev.* **2009**, *38*, 1315−1329.

(5) Zhou, H. C.; Long, J. R.; Yaghi, O. M. Introduction to Metal-Organic Frameworks. *Chem. Rev.* **2012**, *112*, 673−674.

(6) Eddaoudi, M.; Kim, J.; Rosi, N.; Vodak, D.; Wachter, J.; O'Keeffe, M.; Yaghi, O. M. Systematic Design of Pore Size and Functionality in Isoreticular MOFs and Their Application in Methane Storage. *Science* **2002**, *295*, 469−472.

(7) Mahato, P.; Monguzzi, A.; Yanai, N.; Yamada, T.; Kimizuka, N. Fast and Long-Range Triplet Exciton Diffusion in Metal-Organic Frameworks for Photon Upconversion at Ultralow Excitation Power. *Nat. Mater.* **2015**, *14*, 924−930.

(8) Yoon, M.; Srirambalaji, R.; Kim, K. Homochiral Metal-Organic Frameworks for Asymmetric Heterogeneous Catalysis. *Chem. Rev.* **2012**, *112*, 1196−1231.

(9) Jiang, H. X.; Wang, Q. Y.; Wang, H. Q.; Chen, Y. F.; Zhang, M. H. MOF-74 as an Efficient Catalyst for the Low-Temperature Selective Catalytic Reduction of NO_x with NH_3. *ACS Appl. Mater. Interfaces* **2016**, *8*, 26817−26826.

(10) Kuo, C. H.; Tang, Y.; Chou, L. Y.; Sneed, B. T.; Brodsky, C. N.; Zhao, Z. P.; Tsung, C. K. Yolk-Shell Nanocrystal@ZIF-8 Nanostructures for Gas-Phase Heterogeneous Catalysis with Selectivity Control. *J. Am. Chem. Soc.* **2012**, *134*, 14345−14348.

(11) Chen, B. L.; Liang, C. D.; Yang, J.; Contreras, D. S.; Clancy, Y. L.; Lobkovsky, E. B.; Yaghi, O. M.; Dai, S. A Microporous Metal-Organic Framework for Gas-Chromatographic Separation of Alkanes. *Angew. Chem., Int. Ed.* **2006**, *45*, 1390−1393.

(12) Han, S. B.; Wei, Y. H.; Valente, C.; Lagzi, I.; Gassensmith, J. J.; Coskun, A.; Stoddart, J. F.; Grzybowski, B. A. Chromatography in a Single Metal-Organic Framework (MOF) Crystal. *J. Am. Chem. Soc.* **2010**, *132*, 16358−16361.

(13) Iskierko, Z.; Sharma, P. S.; Prochowicz, D.; Fronc, K.; D'Souza, F.; Toczydłowska, D.; Stefaniak, F.; Noworyta, K. Molecularly Imprinted Polymer (MIP) Film with Improved Surface Area Developed by Using Metal-Organic Framework (MOF) for Sensitive Lipocalin (NGAL) Determination. *ACS Appl. Mater. Interfaces* **2016**, *8*, 19860−19865.

(14) Harbuzaru, B. V.; Corma, A.; Rey, F.; Jordá, J. L.; Ananias, D.; Carlos, L. D.; Rocha, J. A Miniaturized Linear pH Sensor Based on a Highly Photoluminescent Self-Assembled Europium(III) Metal-Organic Framework. *Angew. Chem., Int. Ed.* **2009**, *48*, 6476−6479.

(15) Jiang, H. L.; Feng, D. W.; Wang, K. C.; Gu, Z. Y.; Wei, Z. W.; Chen, Y. P.; Zhou, H. C. An Exceptionally Stable, Porphyrinic Zr Metal-Organic Framework Exhibiting pH-Dependent Fluorescence. *J. Am. Chem. Soc.* **2013**, *135*, 13934−13938.

(16) Ma, Y.; Su, H.; Kuang, X.; Li, X. Y.; Zhang, T. T.; Tang, B. Heterogeneous Nano Metal−Organic Framework Fluorescence Probe for Highly Selective and Sensitive Detection of Hydrogen Sulfide in Living Cells. *Anal. Chem.* **2014**, *86*, 11459−11463.

(17) Zhuang, J.; Kuo, C. H.; Chou, L. Y.; Liu, D. Y.; Weerapana, E.; Tsung, C. K. Optimized Metal-Organic Framework Nanospheres for Drug Delivery: Evaluation of Small-Molecule Encapsulation. *ACS Nano* **2014**, *8*, 2812−2819.

(18) He, L. C.; Liu, Y.; Liu, J. Z.; Xiong, Y. S.; Zheng, J. Z.; Liu, Y. L.; Tang, Z. Y. Core-Shell Noble-Metal@Metal-Organic-Framework Nanoparticles with Highly Selective Sensing Property. *Angew. Chem., Int. Ed.* **2013**, *52*, 3741−3745.

(19) Wang, Y.; Yang, J.; Liu, Y. Y.; Ma, J. F. Controllable Syntheses of Porous Metal-Organic Frameworks: Encapsulation of Ln^{III} Cations for Tunable Luminescence and Small Drug Molecules for Efficient Delivery. *Chem. - Eur. J.* **2013**, *19*, 14591−14599.

(20) Panella, B.; Hirscher, M.; Pütter, H.; Müller, U. Hydrogen Adsorption in Metal-Organic Frameworks: Cu-MOFs and Zn-MOFs Compared. *Adv. Funct. Mater.* **2006**, *16*, 520−524.

(21) Rowsell, J. L. C.; Yaghi, O. M. Strategies for Hydrogen Storage in Metal-Organic Frameworks. *Angew. Chem., Int. Ed.* **2005**, *44*, 4670−4679.

(22) Dincă, M.; Long, J. R. Hydrogen Storage in Microporous Metal-Organic Frameworks with Exposed Metal Sites. *Angew. Chem., Int. Ed.* **2008**, *47*, 6766−6779.

(23) Zheng, H. Q.; Zhang, Y. N.; Liu, L. F.; Wan, W.; Guo, P.; Nystrom, A. M.; Zou, X. D. One-pot Synthesis of Metal-Organic Frameworks with Encapsulated Target Molecules and Their Applications for Controlled Drug Delivery. *J. Am. Chem. Soc.* **2016**, *138*, 962−968.

DOI: 10.1021/acsami.6b14446
ACS Appl. Mater. Interfaces 2017, 9, 2150−2158

(24) Meek, S. T.; Greathouse, J. A.; Allendorf, M. D. Metal-Organic Frameworks: A Rapidly Growing Class of Versatile Nanoporous Materials. *Adv. Mater.* **2011**, *23*, 249−267.
(25) Nazari, M.; Rubio-Martinez, M.; Tobias, G.; Barrio, J. P.; Babarao, R.; Nazari, F.; Konstas, K.; Muir, B. W.; Collins, S. F.; Hill, A. J.; Duke, M. C.; Hill, M. R. Metal-Organic-Framework-Coated Optical Fibers as Light-Triggered Drug Delivery Vehicles. *Adv. Funct. Mater.* **2016**, *26*, 3244−3249.
(26) Horcajada, P.; Chalati, T.; Serre, C.; Gillet, B.; Sebrie, C.; Baati, T.; Eubank, J. F.; Heurtaux, D.; Clayette, P.; Kreuz, C.; Chang, J. S.; Hwang, Y. K.; Marsaud, V.; Bories, P. N.; Cynober, L.; Gil, S.; Férey, G.; Couvreur, P.; Gref, R. Porous Metal-Organic-Framework Nanoscale Carriers as a Potential Platform for Drug Delivery and Imaging. *Nat. Mater.* **2010**, *9*, 172−178.
(27) Della Rocca, J.; Liu, D. M.; Lin, W. B. Nanoscale Metal Organic Frameworks for Biomedical Imaging and Drug Delivery. *Acc. Chem. Res.* **2011**, *44*, 957−968.
(28) Kreno, L. E.; Leong, K.; Farha, O. K.; Allendorf, M.; Van Duyne, R. P.; Hupp, J. T. Metal Organic Framework Materials as Chemical Sensors. *Chem. Rev.* **2012**, *112*, 1105−1125.
(29) Horcajada, P.; Serre, C.; Vallet-Regí, M.; Sebban, M.; Taulelle, F.; Férey, G. Metal−Organic Frameworks as Efficient Materials for Drug Delivery. *Angew. Chem., Int. Ed.* **2006**, *45*, 5974−5978.
(30) Ling, P. H.; Lei, J. P.; Jia, L.; Ju, H. X. Platinum Nanoparticles Encapsulated Metal-Organic Frameworks for the Electrochemical Detection of Telomerase Activity. *Chem. Commun.* **2016**, *52*, 1226−1229.
(31) Taylor-Pashow, K. M. L.; Rocca, J. D.; Xie, Z. G.; Tran, S.; Lin, W. B. Postsynthetic Modifications of Iron-Carboxylate Nanoscale Metal-Organic Frameworks for Imaging and Drug Delivery. *J. Am. Chem. Soc.* **2009**, *131*, 14261−14263.
(32) Tian, J. W.; Luo, Y. P.; Huang, L. W.; Feng, Y. Q.; Ju, H. X.; Yu, B. Y. Pegylated Folate and Peptide-Decorated Graphene Oxide Nanovehicle for in Vivo Targeted Delivery of Anticancer Drugs and Therapeutic Self-Monitoring. *Biosens. Bioelectron.* **2016**, *80*, 519−524.
(33) Yan, J.; Hu, C. Y.; Wang, P.; Zhao, B.; Ouyang, X. Y.; Zhou, J.; Liu, R.; He, D. N.; Fan, C. H.; Song, S. P. Growth and Origami Folding of DNA on Nanoparticles for High-Efficiency Molecular Transport in Cellular Imaging and Drug Delivery. *Angew. Chem., Int. Ed.* **2015**, *54*, 2431−2435.
(34) Lukyanov, A. N.; Torchilin, V. P. Micelles from Lipid Derivatives of Water-Soluble Polymers as Delivery Systems for Poorly Soluble Drugs. *Adv. Drug Delivery Rev.* **2004**, *56*, 1273−1289.
(35) Szakács, G.; Paterson, J. K.; Ludwig, J. A.; Booth-Genthe, C.; Gottesman, M. M. Targeting Multidrug Resistance in Cancer. *Nat. Rev. Drug Discovery* **2006**, *5*, 219−234.
(36) Wang, J. J.; Zhang, L. W.; Chen, M. L.; Gao, S.; Zhu, L. Activatable Ferritin Nanocomplex for Real-Time Monitoring of Caspase-3 Activation during Photodynamic Therapy. *ACS Appl. Mater. Interfaces* **2015**, *7*, 23248−23256.
(37) Zhang, L.; Lei, J. P.; Ma, F. J.; Ling, P. H.; Liu, J. T.; Ju, H. X. A Porphyrin Photosensitized Metal-Organic Framework for Cancer Cell Apoptosis and Caspase Responsive Theranostics. *Chem. Commun.* **2015**, *51*, 10831−10834.
(38) Lovell, J. F.; Liu, T. W. B.; Chen, J.; Zheng, G. Activatable Photosensitizers for Imaging and Therapy. *Chem. Rev.* **2010**, *110*, 2839−2857.
(39) Agostinis, P.; Berg, K.; Cengel, K. A.; Foster, T. H.; Girotti, A. W.; Gollnick, S. O.; Hahn, S. M.; Hamblin, M. R.; Juzeniene, A.; Kessel, D.; Korbelik, M.; Moan, J.; Mroz, P.; Nowis, D.; Piette, J.; Wilson, B. C.; Golab, J. Photodynamic Therapy of Cancer: An Update. *Ca-Cancer J. Clin.* **2011**, *61*, 250−281.
(40) Park, J.; Jiang, Q.; Feng, D. W.; Mao, L. Q.; Zhou, H. C. Size-Controlled Synthesis of Porphyrinic Metal-Organic Framework and Functionalization for Targeted Photodynamic Therapy. *J. Am. Chem. Soc.* **2016**, *138*, 3518−3525.
(41) Lu, K. D.; He, C. B.; Lin, W. B. Nanoscale Metal-Organic Framework for Highly Effective Photodynamic Therapy of Resistant Head and Neck Cancer. *J. Am. Chem. Soc.* **2014**, *136*, 16712−16715.
(42) Lu, K. D.; He, C. B.; Lin, W. B. A Chlorin-Based Nanoscale Metal Organic Framework for Photodynamic Therapy of Colon Cancers. *J. Am. Chem. Soc.* **2015**, *137*, 7600−7603.
(43) Henderson, B. W.; Fingar, V. H. Relationship of Tumor Hypoxia and Response to Photodynamic Treatment in an Experimental Mouse Tumor. *Cancer Res.* **1987**, *47*, 3110−3114.
(44) Liu, Y. Y.; Liu, Y.; Bu, W. B.; Cheng, C.; Zuo, C. J.; Xiao, Q. F.; Sun, Y.; Ni, D. L.; Zhang, C.; Liu, J. N.; Shi, J. L. Hypoxia Induced by Upconversion-Based Photodynamic Therapy: Towards Highly Effective Synergistic Bioreductive Therapy in Tumors. *Angew. Chem., Int. Ed.* **2015**, *54*, 8105−8109.
(45) Brown, J. M.; Wilson, W. R. Exploiting Tumor Hypoxia in Cancer Treatment. *Nat. Rev. Cancer* **2004**, *4*, 437−447.
(46) Zhang, C.; Zhao, K. L.; Bu, W. B.; Ni, D. L.; Liu, Y. Y.; Feng, J. W.; Shi, J. L. Marriage of Scintillator and Semiconductor for Synchronous Radiotherapy and Deep Photodynamic Therapy with Diminished Oxygen Dependence. *Angew. Chem., Int. Ed.* **2015**, *54*, 1770−1774.
(47) Fitzgerald, J. B.; Schoeberl, B.; Nielsen, U. B.; Sorger, P. K. Systems Biology and Combination Therapy in the Quest for Clinical Efficacy. *Nat. Chem. Biol.* **2006**, *2*, 458−466.
(48) Son, K. J.; Yoon, H. J.; Kim, J. H.; Jang, W. D.; Lee, Y.; Koh, W. G. Photosensitizing Hollow Nanocapsules for Combination Cancer Therapy. *Angew. Chem., Int. Ed.* **2011**, *50*, 11968−11971.
(49) Canti, G.; Nicolin, A.; Cubeddu, R.; Taroni, P.; Bandieramonte, G.; Valentini, G. Antitumor Efficacy of the Combination of Photodynamic Therapy and Chemotherapy in Murine Tumors. *Cancer Lett.* **1998**, *125*, 39−44.
(50) Chen, R.; Zhang, J. F.; Wang, Y.; Chen, X. F.; Zapien, J. A.; Lee, C. S. Graphitic Carbon Nitride Nanosheet@Metal-Organic Framework Core-Shell Nanoparticles for Photo-Chemo Combination Therapy. *Nanoscale* **2015**, *7*, 17299−17305.
(51) Peng, C. L.; Shieh, M. J.; Tsai, M. H.; Chang, C. C.; Lai, P. S. Self-Assembled Star-Shaped Chlorin-Core Poly(ε-Caprolactone)-Poly(Ethyleneglycol) Diblock Copolymer Micelles for Dual Chemo-Photodynamic Therapies. *Biomaterials* **2008**, *29*, 3599−3608.
(52) He, C. B.; Liu, D. M.; Lin, W. B. Self-Assembled Core-Shell Nanoparticles for Combined Chemotherapy and Photodynamic Therapy of Resistant Head and Neck Cancers. *ACS Nano* **2015**, *9*, 991−1003.
(53) Son, K. J.; Yoon, H. J.; Kim, J. H.; Jang, W. D.; Lee, Y.; Koh, W. G. Photosensitizing Hollow Nanocapsules for Combination Cancer Therapy. *Angew. Chem., Int. Ed.* **2011**, *50*, 11968−11971.
(54) Tian, J. W.; Ding, L.; Ju, H. X.; Yang, Y. C.; Li, X. L.; Shen, Z.; Zhu, Z.; Yu, J. S.; Yang, C. J. A Multifunctional Nanomicelle for Real-Time Targeted Imaging and Precise Near-Infrared Cancer Therapy. *Angew. Chem., Int. Ed.* **2014**, *53*, 9544−9549.
(55) Russo, A.; Bazan, V.; Gebbia, N.; Pizzolanti, G.; Tumminello, F. M.; Dardanoni, G.; Ingria, F.; Restivo, S.; Tomasino, R. M.; Leto, G. Flow Cytometric DNA Analysis and Lysosomal Cathepsins B and L in Locally Advanced Laryngeal Cancer. *Cancer* **1995**, *76*, 1757−1764.
(56) Lah, T. T.; Čerček, M.; Blejec, A.; Kos, J.; Gorodetsky, E.; Somers, R.; Daskal, I.; Cathepsin, B. a Prognostic Indicator in Lymph Node-negative Breast Carcinoma Patients: Comparison with Cathepsin D, Cathepsin L, and Other Clinical Indicators. *Clin. Cancer Res.* **2000**, *6*, 578−584.
(57) Nishikawa, H.; Ozaki, Y.; Nakanishi, T.; Blomgren, K.; Tada, T.; Arakawa, A.; Suzumori, K. The Role of Cathepsin B and Cystatin C in the Mechanisms of Invasion by Ovarian Cancer. *Gynecol. Oncol.* **2004**, *92*, 881−886.
(58) Bengsch, F.; Buck, A.; Günther, S. C.; Seiz, J. R.; Tacke, M.; Pfeifer, D.; von Elverfeldt, D.; Sevenich, L.; Hillebrand, L. E.; Kern, U.; Sameni, M.; Peters, C.; Sloane, B. F.; Reinheckel, T. Cell Type-Dependent Pathogenic Functions of Overexpressed Human Cathepsin B in Murine Breast Cancer Progression. *Oncogene* **2014**, *33*, 4474−4484.
(59) Page, A. E.; Warburton, M. J.; Chambers, T. J.; Pringle, J. A. S.; Hayman, A. R. Human Osteoclastomas Contain Multiple Forms of Cathepsin B. *Biochim. Biophys. Acta, Gen. Subj.* **1992**, *1116*, 57−66.

DOI: 10.1021/acsami.6b14446
ACS Appl. Mater. Interfaces 2017, 9, 2150−2158

(60) Wu, B.; Lin, X. C.; Ge, L.; Wu, L.; Xu, T. W. A Novel Route for Preparing Highly Proton Conductive Membrane Materials with Metal-Organic Frameworks (MOFs). *Chem. Commun.* **2013**, *49*, 143−145.
(61) Zhu, Z.; Tang, Z. W.; Phillips, J. A.; Yang, R. H.; Wang, H.; Tan, W. H. Regulation of Singlet Oxygen Generation Using Single-Walled Carbon Nanotubes. *J. Am. Chem. Soc.* **2008**, *130*, 10856−10857.
(62) Jin, H.; Yang, P. H.; Cai, J. Y.; Wang, J. H.; Liu, M. Photothermal Effects of Folate-Conjugated Au Nanorods on HepG2 Cells. *Appl. Microbiol. Biotechnol.* **2012**, *94*, 1199−1208.
(63) Zhu, X.; Zheng, H. Y.; Wei, X. F.; Lin, Z. Y.; Guo, L. H.; Qiu, B.; Chen, G. N. Metal-Organic Framework (MOF): a Novel Sensing Platform for Biomolecules. *Chem. Commun.* **2013**, *49*, 1276−1278.
(64) Kim, S.; Fujitsuka, M.; Majima, T. Photochemistry of Singlet Oxygen Sensor Green. *J. Phys. Chem. B* **2013**, *117*, 13985−13992.

DOI: 10.1021/acsami.6b14446
ACS Appl. Mater. Interfaces 2017, 9, 2150−2158